EISEVIER

Contents lists available at ScienceDirect

Journal of Colloid and Interface Science

journal homepage: www.elsevier.com/locate/jcis



Regular Article

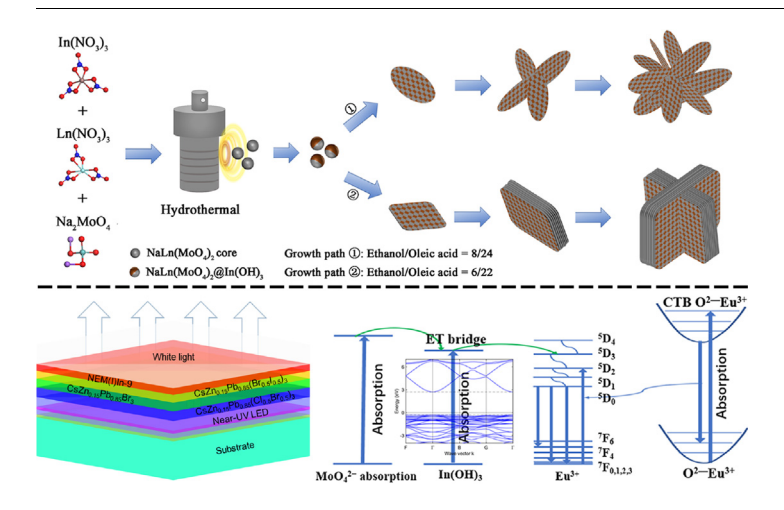
Enhanced luminescence through interface energy transfer in hierarchical heterogeneous nanocomposites and application in white LEDs



Guoyang Gao^a, Yini Li^a, Wenjing Yu^a, Guofeng Wang^{a,*}, Peifen Zhu^{b,*}, Weiping Qin^c, Dingsheng Wang^d

- a Key Laboratory of Functional Inorganic Material Chemistry, Ministry of Education, School of Chemistry and Materials Science, Heilongjiang University, Harbin 150080, China
- ^b Department of Physics and Engineering Physics, The University of Tulsa, Tulsa, OK 74104, USA
- ^c College of Electronic Science and Engineering, Jilin University, 120012, China
- ^d Department of Chemistry, Tsinghua University, Beijing 100084, China

G R A P H I C A L A B S T R A C T



ARTICLE INFO

Article history: Received 19 August 2020 Revised 9 September 2020 Accepted 14 September 2020 Available online 23 September 2020

Keywords: Luminous enhancement Lanthanide NaLn(MoO₄)₂@In(OH)₃ white LEDs

ABSTRACT

Highly efficient light-emitting materials are essential for achieving high-performance devices. Here, a novel composite system, as well as enhanced luminescence processes, was designed, where NaLn (MoO₄)₂ ultra-small nucleus can be effectively isolated by $\ln(OH)_3$ to form $\ln(OO_4)_2$ $\ln(OO_4)_2$ and $\ln(OO_4)_3$ composite nanoclusters due to the different nucleation rate between $\ln(OO_4)_2$ and $\ln(OO_4)_3$, and then these small composite clusters gradually self-assemble into hierarchical structures. As we expected, the enhanced luminescence was achieved from hierarchical $\ln(OO_4)_2$ nanostructures with adjusting the distance among $\ln(OO_4)_2$ ultra-small nucleus by inserting $\ln(OO_4)_2$. A series of spectroscopy results show that the $\ln(OO_4)_3$ not only acts as an energy transfer bridge from CTB $\ln(OO_4)_4$ and change the J-O parameters. The Raman peak at 134 cm⁻¹ is helpful to populate the $\ln(OO_4)_4$ level of $\ln(OO_4)_4$ or the excited states of $\ln(OO_4)_4$ resulting in stronger up/down-conversion emissions. The use of NaLn ($\ln(OO_4)_2$ $\ln(OO_4)_3$ with blue, green, and yellow emission from halide perovskites could achieve white light with excellent vision performance (an LER of 376 $\ln(OO_4)_4$) and superior color

E-mail addresses: wanggf_w@163.com (G. Wang), peifen-zhu@utulsa.edu (P. Zhu).

^{*} Corresponding authors.

quality (CRI > 92). The findings of this experiment provide a new idea for the design of composite interface materials

© 2020 Elsevier Inc. All rights reserved.

1. Introduction

Lanthanide-doped fluorescent nanomaterials have drawn extensive attention because they possess unique optical properties including narrow emission bandwidth, large Stokes shift, high resistance to optical blinking, superior high-to-low energy photon conversion efficiency and vice versa [1–11]. Thus, they have shown a great deal of interest for their potential applications in various fields such as sensing, imaging, lighting, photocatalysis, and display [12-26]. One of the most typical ones is the multicolor dual-mode luminescence and strong upconverting and downshifting emissions of core@multi-shell lanthanide-doped nanomaterials for complex information storage by precisely controlling the distribution of lanthanide elements in the core and distinct shell layers. It is of great significance in the fields of advanced anticounterfeiting and solid-state lighting [27]. Nevertheless, one noteworthy roadblock still exists: most of the up-conversion (UC) and down-conversion (DC) luminescence nanomaterials fell through producing superior luminescence efficiency, which immensely limits the practical application in various fields. For example, owing to the lower emission signal, penetration depth in biomarkers and bioimaging will be severely limited [28-32]. Therefore, to solve such practical problems and fully realize their potentials, it is imperative to study more efficient lanthanidedoped luminescent materials [33-35].

As regards the practical applications based on UC or DC luminescence, enhancing the luminescence intensity has become a research focus [36-38]. Studies have shown that UC nanomaterials often have low-emission efficiency resulted from structural defects, higher phonon energy, small absorption cross-sections of activator ions, and parity-forbidden transition of rare-earth ions. Therefore, overcoming the above limitation has become the main work of researchers. Typically, Song et al. achieved 144-fold UCL improvement of Cs_xWO₃/NaYF₄/NaYF₄: Yb³⁺, Er³⁺ hybrid by constructing a core-shell structure and using plasma semiconductors [39]. Until now, various methods have been employed to improve luminescence efficiency of nanomaterials including adjusting matrix and doping ions, surface modification by using core-shell structures, metal surface Plasmon resonance (SPR) enhancement, co-doping transition metal ions with lanthanide ions, introducing the synergistic sensitizers to reduce the thermal effect, and synergistic effect of organic dyes and UCNPs [40-45]. Among them, surface modification is considered to be one of the most effective methods [46,47]. Most importantly, the enhancement of luminescence intensity by surface modification using hydroxide as a surface shell has never been reported.

It is well known that the physical and chemical properties of materials strongly depend on the microstructure of materials. Although the traditional step-by-step synthesis method for the composites can modify the surface of the core material to a certain extent, it cannot effectively adjust the microstructure of the core material. In this work, we designed a novel composite system as well as a new energy transfer (ET) and enhanced luminescence processes, as shown in Scheme 1. By using this novel design, NaLn(MoO₄)₂ ultra-small nucleus can be effectively isolated by In (OH)₃ to form NaLn(MoO₄)₂@In(OH)₃ composite nanoclusters due to the different nucleation rate between NaLn(MoO₄)₂ and In (OH)₃, and then these small composite clusters gradually self-assemble into hierarchical structures. The enhanced UC/DC lumi-

nescence of hierarchical NaLn(MoO₄)₂ nanostructures was achieved with adjusting nanocluster distance by inserting In (OH)₃ among NaLn(MoO₄)₂@In(OH)₃ composite nanoclusters. The mechanisms for the experimentally observed enhancement in UC/DC luminescence were clarified and we were able to adequately illustrate the effect of the spatial relationships between NaLn(MoO₄)₂ and In(OH)₃ on the UC/DC emissions with a particular condition. To explore the potential applications of NaLn (MoO₄)₂@In(OH)₃ in white light-emitting diodes (LEDs), red emission from Eu-NaY(MoO₄)₂@In(OH)₃ was combined with blue, green, and yellow emission from perovskites to obtain white light. The white light with superior color quality and excellent vision performance was obtained. As more excellent multicolor fluorescent materials, NaLn(MoO₄)₂@In(OH)₃ hybrid nanostructures have shown broader application prospects in the fields of fluorescent probes, laser dyes, and LED devices.

2. Materials and methods

The chemicals used in this experiment in supporting information.

Synthesis of NaLn(MoO₄)₂. 1.2 g NaOH was dissolved in 4 mL deionized water, and subsequently, the solution was mixed with ethanol (8 mL) and OA (24 mL) under constant stirring. Afterward, $Ln(NO_3)_3$ (Ln = Yb/Er, Eu and Tb (0.5 mol/L)) and Na_2MoO_4 (1 mol/L) aqueous solutions were dropped into the above mixture and stirred for 40 min. The colloidal solution was hydrotreated at 180 °C for 24 h. After the systems are cooled down, the products were obtained employing centrifugation and washed three times.

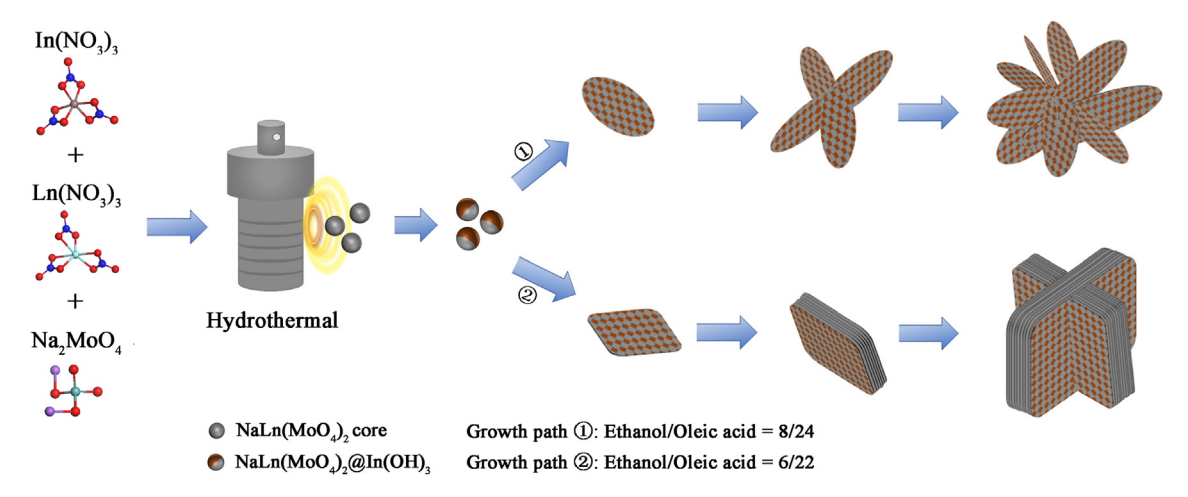
Synthesis of $NaLn(MoO_4)_2@In(OH)_3$. Similarly, $Ln(NO_3)_3$ (Ln = Yb/Er, Eu and Tb (0.5 mol/L)) and Na_2MoO_4 (1 mol/L) aqueous solutions were dropped into the mixture of NaOH, deionized water, ethanol and oleic acid with continuous stirring. After stirring for 10 min, the equimolar ratio of $In(NO_3)_3$ (0.5 mol/L) to NaOH mixed aqueous solution was dropped into the above system and stirred for about 40 min. The colloidal solution was hydrotreated at different temperatures (160, 180, and 200 °C) and time (12, 18, 24, and 30 h). The other experimental steps are the same as above. The molar ratio of the reaction materials is shown in Table S1 and S2.

Characterization details and spectral optimization of white light from $NaLn(MoO_4)_2@In(OH)_3$ hybrid nanostructures are shown in the supporting information.

3. Results and discussion

3.1. Design scheme of overall work

As mentioned above, to modify the surface and interior of the $NaLn(MoO_4)_2$ material at the same time, to obtain new $NaLn(MoO_4)_2@In(OH)_3$ composites with excellent physical and chemical properties, we boldly designed a one-step synthesis strategy by controlling the nucleation rate of different materials, as shown in Scheme 1. $NaLn(MoO_4)_2$ nanocrystals nucleate first, and then In $(OH)_3$ grows on the surface of $NaLn(MoO_4)_2$ cores, because of the different nucleation rate between $NaLn(MoO_4)_2$ and $In(OH)_3$. With increasing reaction time, the ultra-small $NaLn(MoO_4)_2@In(OH)_3$ nanoparticles gradually self-assemble into nanochips, and then further self-assemble into hierarchical structures, which will be



Scheme 1. $NaLn(MoO_4)_2$ nanoclusters can be effectively isolated by $In(OH)_3$ to form $NaLn(MoO_4)_2@In(OH)_3$ nanoclusters, and then the ultra-small clusters gradually self-assemble into hierarchical structures.

proved and discussed in detail later. And thus, the distance among clusters can be adjusted by adjusting the initial content of In $(NO_3)_2$.

As we predicted, the enhanced luminescence was achieved from hierarchical $NaLn(MoO_4)_2$ nanostructures with adjusting $NaLn(MoO_4)_2$ nanocluster distance by inserting $In(OH)_3$, which were synthesized by a simple one-pot hydrothermal method based on self-assembly of two-dimensional nanosheets, which will be described and discussed later in detail.

3.2. Morphology and structure analysis

The morphology, size, and crystal phase purity of the prepared hybrid nanostructures are discussed in detail below depending on conditions including reaction temperature and time, reactant concentration, and solvent volume ratio.

The detailed synthesis information, sample abbreviation, and CIE chromaticity coordinates are listed in Table S1 in the Electronic Supplementary Information (ESI). First, the effects of the solvent volume ratio on the size, morphology, and crystal structure of the as-prepared hybrid nanostructures have been studied by changing the volume ratio of ethanol to oleic acid. Fig. 1 shows SEM (a) and TEM (b) images of NYME(I)@In-8 synthesized at 180 °C. It shows the morphology of nanoflowers consisting of two-dimensional nanosheets of approximately 800 nm in the lateral dimension for using ethanol and oleic acid volume of 8 mL and 24 mL, respectively. Interestingly, when the volume of ethanol and oleic acid was changed to 6 mL and 24 mL, respectively, the morphology of the samples changed significantly. The SEM (Fig. 1c) and TEM (Fig. 1d) images indicate that the morphology of NYME(II)@In-8 is the square nano-sandwiches-plus structure of approximately 400 nm in the lateral dimension. The experimental results indicated that the solvent volume ratio affects morphology and size. However, the XRD patterns (Fig. S1) confirmed that the crystal structure is unaffected by the morphology of the samples. The HRTEM images show that the two-phase materials are cross distributed in the material, which further proves that the composite began to form at the nucleation stage, and then formed a flower-like hierarchical structure through self-assembly (Fig. 1e). Moreover, the two-dimensional element-mapping images of NYME (I)@In-8 (Fig. 1f) illustrate that all elements are uniformly distributed in the prepared samples. In addition, Fig. S2 and Fig. S3 show the SEM element-mapping images of NYME(II) and NYME (II)@In-9 respectively, showing a very uniform distribution for all elements.

The influence of hydrothermal temperature and time have been studied for lanthanide-doped nanocrystals in this work and see the supplementary information for a detailed discussion (Fig. S(4–6)). Noteworthily, it can be seen from the corresponding XRD patterns (Fig. S7) that too short time is not conducive to the formation of In (OH)₃, indicating that the nucleation rate of NaLn(MoO₄)₂ cores is relatively faster compared to that of In(OH)₃. The diffraction peaks become narrower with increasing hydrothermal time, indicating the increased crystallinity and size with time, which is consistent with the SEM results. See the supplementary information for the effect of hydrothermal time on NYME(II)@In-8 (Fig. S8).

The XRD patterns of NEM(I), NEM(I)@In-9, NYME(I), NYME(I) @In-8 are shown in Fig. 1g. Note that the coating of In(OH)3 did not cause the shift of diffraction peaks from NaLn(MoO₄)₂. Interestingly, the XRD patterns of NaLn(MoO₄)₂@In(OH)₃ become narrower gradually compared with those of NaLn(MoO₄)₂, proving that NaLn(MoO₄)₂ ultra-small nucleus can be effectively isolated by In(OH)₃ to form NaLn(MoO₄)₂@In(OH)₃ composite nanoclusters (Fig. 1g). Thermogravimetric analysis (TGA) was used to evaluate the stability of as-synthesized samples (Fig. S9). The assynthesized samples exhibit excellent thermal stability in the range of 40 °C to 800 °C. When the temperature is 150 °C, the trace weight loss of the samples is mainly due to the evaporation of the adsorbed water. Only when the temperature exceeds 640 °C, In (OH)₃ surface molecules are dehydrated and transforms into oxides, which leads to a slightly larger weight loss of NEM(I)@In-9 than NEM(I). Thus, NEM(I)@In-9 shows excellent thermal stability. Such high thermal decomposition temperature makes the NEM(I) @In-9 suitable for white LED applications.

Fourier transform infrared (FT-IR) spectroscopy measurement was carried out to determine the functional groups on the surface of the samples, which give supporting proof for the successful fabrication of the samples. As shown in Fig. S10, broadband at ~3420 cm⁻¹ is observed for all four samples, which could be associated with the O—H stretching vibration. The peak at 2450 cm⁻¹ is attributed to the stretching vibration of residual carboxylate ions on the surface of the samples. The characteristic peaks of NaLn (MoO₄)₂ appear at 911 and 780 cm⁻¹, which are caused by the asymmetric and symmetric stretching vibrations of the Mo=O and Mo-O, respectively. What's more, the characteristic peak arising from the Mo-O-Mo stretching vibrations appears at 699 nm. The additional peak at 1154 cm⁻¹ for In(OH)₃ coated NaLn(MoO₄)₂ is associated with the deformation vibrations of the In - OH bond. Thus, we have successfully obtained the NaLn(MoO₄)₂@In(OH)₃ hybrid nanostructures.

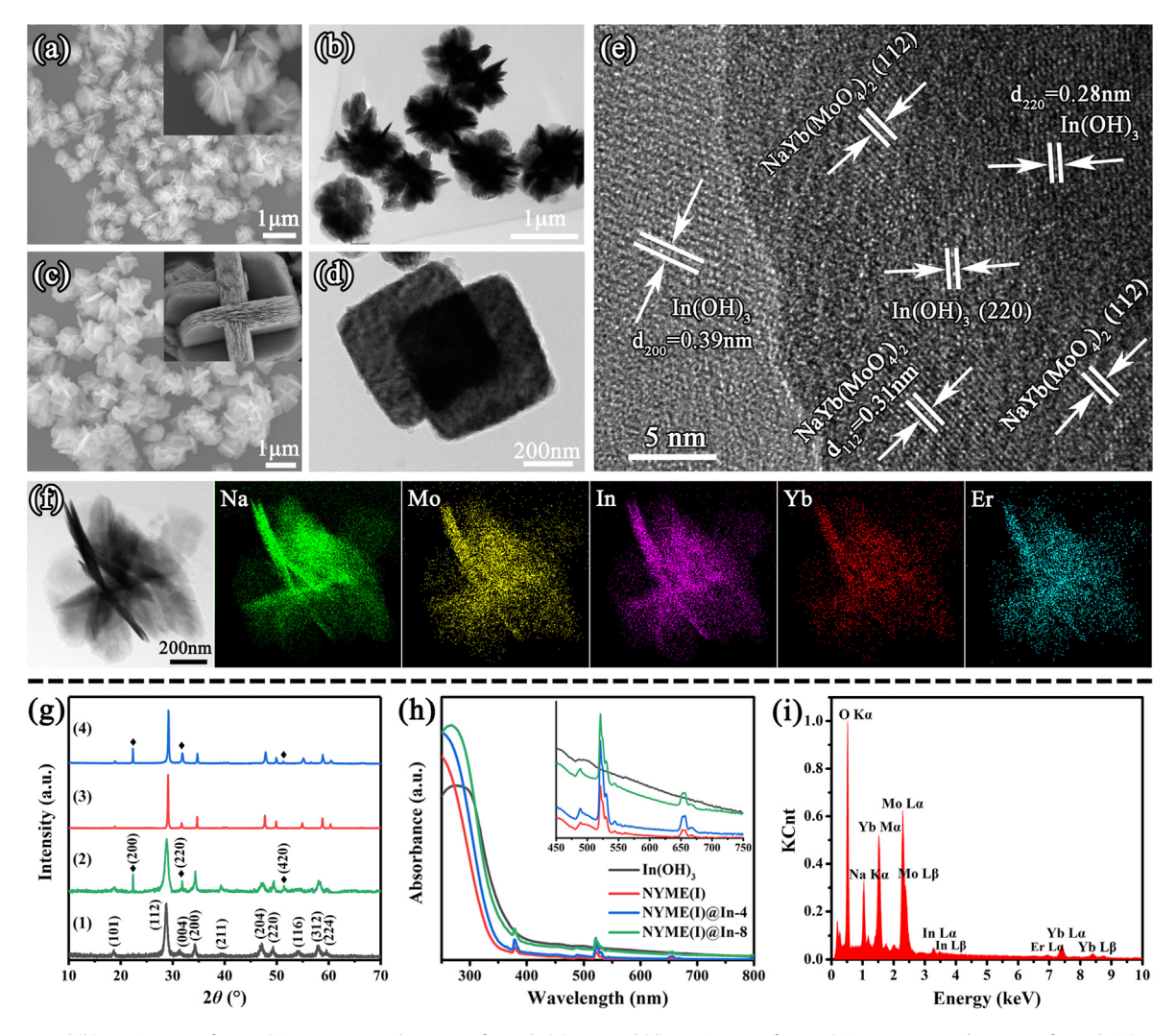


Fig. 1. (a) SEM and (b) TEM images of NYME(I)@In-8 prepared at 180 °C for 24 h. (c) SEM and (d)TEM images of NYME(II)@In-8 prepared at 180 °C for 24 h. (e) HRTEM images of NYME(I)@In-8 prepared at 180 °C for 24 h. (f) the elemental mapping images of Na, Mo, In, Yb, and Er in NYME(I)@In-8. (g) XRD patterns of (1) NEM(I), (2) NEM(I)@In-9, (3) NYME(I), and (4) NYME(I)@In-8. (h) UV-vis absorption spectra of In(OH)3, NYME(I)@In-4, NYME(I)@In-8. (i) EDS spectra of NYME(I)@In-8.

Fig. 1h shows the UV-vis absorption spectra of In(OH)₃, NYME (I), NYME(I)@In-4, and NYME(I)@In-8. The strong absorption of NYME(I) at less than 400 nm indicates that the range of absorption light is principally in the ultraviolet (UV) region. The distinct absorption peaks at 378, 521, and 657 nm are mainly caused by rare-earth ions. The intensity of the absorption peaks also increased greatly. As the surface of the samples is compounded with In(OH)3, the absorption peaks move toward the visible light region. The ultraviolet absorption edge of In(OH)₃ exhibits an obvious redshift, which is greatly affected by the synthesis conditions. Our experimental results are consistent with those previously reported [48]. Fig. S11 shows near-infrared absorption spectra of In(OH)3, NYME(I), and NYME(I)@In-8. The absorption peak intensity of NYME(I)@In-8 at 980 nm is significantly enhanced compared to NYME(I). This will promote the material to absorb the light more efficiently, thereby enhancing its luminous intensity. In short, the compounding In(OH)₃ resulted in enhanced absorption and emission, which in turn proves that the samples are successfully compounded by In(OH)₃.

The EDX spectrum of the hybrid nanostructures is shown in Fig. 1i, which indicates that Na, Mo, O, Yb, Er, and In are all present in NYME(I)@In-8 sample. This further proves that the NYME(I)@In-8 hybrid nanostructures had been successfully obtained. The EDX

analysis on the NYME(II) (Fig. S12) shows that NYME(II) consists of elements of Na, Mo, O, Yb, and Er.

Raman scattering measurements were carried out on NYME(I) @In-8 nanostructures to elucidate the structural characteristics and interaction between NaYb(MoO₄)₂ and In(OH)₃. Four main scattering peaks are present in the range of 100-1100 cm⁻¹ as shown in Fig. S13. The peak at 134 cm⁻¹ is related to In -OH, which is originated from the bending vibration of the In(OH)₃ octahedron [49]. It is noted that the luminescence intensity of the sample is related to the process of nonradiative relaxation, phononassisted energy transfer, and so on. All these processes are related to the phonon energy, and thus, the additional phonon mode of In (OH)₃ is helpful to enhance the luminescence intensity of the samples, which will be discussed in detail later. The Raman shifts at $^{-3}$ 25 and 400 cm $^{-1}$ resulted from the twofold degenerate $\rm E_a$ symmetric bending mode and the F_{2g} asymmetric bending mode of the MoO₄ units, respectively. The high-frequency Raman shift at 879 cm⁻¹ is specified as the symmetric A_{1g} stretching mode of the MoO₄ units. A superimposed peak at 831 cm⁻¹ caused by the F_{2g} asymmetric stretching mode is also detected [50].

The XPS survey spectrum revealed that the tested sample was composed of Na, Mo, O, In, Yb, Er, and adventitious carbon (Fig. S14). The XPS survey spectrum of NEM(I)@In-9 is shown in

Fig. S15, which evidences the existence of Na, Mo, O, In, and Eu elements. The presence of the C element is due to surface contamination. See the supplementary information for more detailed discussions (Fig. S16 and Fig. S17). It could be calculated that the valence-band edge positions of the NYME(I)@In-8 and NEM(I) @In-9 are approximately 2.20 eV and 2.01 eV, respectively (Fig S18). It is noted that the results of the EDS spectrum indicated that the In³⁺/Ln³⁺ molar ratio of NYME(I)@In-8 is 0.11. However, the results of the XPS spectrum indicated that the In³⁺/Ln³⁺ molar ratio of NYME(I)@In-8 is 0.16. It is well known that the detection depth of EDS test technology is deeper than that of XPS test technology. The results mentioned above indicates that the content of In on the surface is higher than that in the body. Thus, NaLn(MoO₄)₂ is the cores and In(OH)₃ is the shells in NaLn(MoO₄)₂@In(OH)₃ composites, which is consistent with the assumed growth mechanism. The element analysis of NYME(I)@In-8 was performed to analyze the element content more accurately by ICP-OES and CHNSO technique. The result was listed in Table S4 that the element content of Na, Mo, Yb, Er, and In are 2.60, 4,27, 1.38, 0.19, and 0.48 mol/Kg, respectively.

3.3. Luminescence properties

Na₂MoO₄ is a material with lower phonon energy, thus it can serve as an efficient host lattice for the DC luminescence process. Fig. S19a presents the photographs of as-prepared NaLn(MoO₄)₂@-In-9 (Ln = Eu, Tb, and Eu/Tb) samples synthesized with different Eu³⁺/Tb³⁺ molar ratios and different emission colors were observed by tuning of Eu³⁺/Tb³⁺ molar ratios. Specifically, we obtained red, orange, yellow, and green emission by simply adjusting the Eu³⁺/ Tb³⁺ molar ratios to 8:0, 5:3, 3:5, and 0:8, respectively. The emission spectra of four typical samples excited by 290-nm light are shown in Fig. S19b. It can be seen from the graph that the samples yield the characteristic emissions of Tb³⁺ ions at 494, 549, 587, and 622 nm, which correspond to the Tb³⁺ transition of 5D_4 - 7F_6 , 5D_4 - $^7F_5,\,^5D_4$ - 7F_4, and 5D_4 - 7F_3, respectively. Similarly, the typical Eu $^{3+}$ emission peaks at 596, 619, 658, and 707 nm were also observed, and these peaks are assigned to the 5D_0 - 7F_1 , 5D_0 - 7F_2 , 5D_0 - 7F_3 , and 5D_0 - 7F_4 transitions of Eu³⁺ ions, respectively.

Next, we studied the influence of $In(OH)_3$ on the fluorescence properties of NEM(I)@In-x (x = 6, 9, and 12) with different molar amounts of $In(OH)_3$. Fig. 2a shows the room-temperature excitation and emission spectra of NEM(I)@In-x (x = 6, 9, and 12). The excitation spectra consist of broadband and several sharp excitation peaks. The broad excitation band in the region between 220 nm and 350 nm is attributed to the overlap of MoO_4^{2-} absorption and CTB $Eu^{3+} \rightarrow O^{2-}$. Compared to NEM(I), the location of the excitation peak red-shift first, and then reverse, which will be discussed later in detail. The sharp excitation peaks are caused by the f-f transition of Eu ions.

Fig. 2a also shows the emission spectra of the NEM(I) with different molar amounts of In(OH)₃ under 467-nm light excitation. The emission peaks are assigned to the following transitions: ⁵D₀ $-{}^{7}F_{1}$ (~596 nm), ${}^{5}D_{0}$ - ${}^{7}F_{2}$ (~619 nm), ${}^{5}D_{0}$ - ${}^{7}F_{3}$ (~658 nm), and 5D_0 - 7F_4 (~708 nm). Among them, the emission peak at 619 nm $(^5D_0 - ^7F_2)$ is the strongest. The strongest emission was observed from NEM(I)@In-9. We suggested that the Raman peaks (Fig. S13) related to In – OH are helpful to the process of nonradiative relaxation from the charge transfer band (CTB) $Eu^{3+} \rightarrow$ O^{2-} to 5D_0 level, which plays a vital role in populating 5D_0 level of Eu³⁺ ions. Thus, the luminescence intensity of the sample was enhanced by coupling In(OH)₃. In addition, the I-O parameters [51] were calculated from the emission spectra of different samples as shown in Table 1. It is well known that the values of Ω_2 are related to the symmetry around Eu3+ ions, which directly affects the intensity of the 5D_0 - 7F_2 emission peak. The results indicated that the symmetry around ${\rm Eu}^{3+}$ ions in NEM@In-9 is the lowest, resulting in the strongest emission peaks. In addition, ${\rm In}({\rm OH})_3$ can enhance both charge transfer transition between ${\rm Eu}^{3+}$ and ${\rm O}^{2-}$ and ${\rm MoO}_4^{2-}$ absorption, which are also factors leading to enhanced fluorescence.

Meanwhile, the emission spectra of NEM(I)@In-9 with different excitation wavelengths are shown in Fig. 2b. The CIE chromaticity coordinates of NEM(I)@In-9 was calculated to be (0.612, 0.311) (Fig. 2b). As a high-quality red-emitting fluorescent material, the sample shows great advantages in the field of LED devices. In addition, the temperature-dependent excitation and emission spectra of NEM(I)@In-9 were studied and the corresponding spectra are shown in Fig. S20. The results show that the temperature has little effect on the luminous intensity, therefore, the NEM(I)@In-9 is suitable for white LED applications. In order to study the DC luminescence properties of Eu3+ in the Na2MoO4@In(OH)3 host, the excitation and emission spectra of hybrid nanostructures with different Eu³⁺ concentrations are recorded and shown in Fig. S21. Upon gradually increasing Eu³⁺ amounts from 0.01 to 0.08 mmol, the fluorescence of samples was increased dramatically. Further increasing amounts from 0.08 to 0.2 mmol, the PL intensity quenched significantly, revealing the concentration quenching feature. The emission was strongest when the Eu³⁺ amount was

As shown in Scheme 2, we assumed that the enhanced luminescence of NEM(I)@In-9 can be caused by the introduction of In(OH)₃ energy transfer (ET) bridge. In order to further study the existence of the energy transfer (ET) bridge from charge transfer band (CTB) $Eu^{3+} \rightarrow O^{2-}$ (or the energy level caused by MoO_4^{2-} absorption) to Eu^{3+} ions, the excitation bands of NEM and NEM(I)@In-x (x = 6, 9, and 12) in the range of 220-350 nm were fitted with two or three Gaussian curves, respectively. The excitation band of NEM can be fitted with two Gaussian curves (Fig. 2c), while the excitation bands of NEM(I)@In-x (x = 6, 9, and 12) can be fitted with three Gaussian curves (Fig. 2(d-f)). For the excitation band of NEM, the two fitted peaks at 283 and 309 nm are attributed to the CTB Eu³⁺ \rightarrow O²⁻ and MoO₄²⁻ absorption, respectively. For the excitation band NEM(I)@In-x, the third fitted peak at 327 nm is attributed to the absorption of In(OH)₃, and the peak intensity ratio of In(OH)₃/CTB increases with increasing the molar amounts of In (OH)₃. However, with increasing the molar amounts of In(OH)₃, the peak intensity ratio MoO_4^{2-}/CTB increases first and then decreases. When the In(OH)₃ content is low, the In(OH)₃ tends to be the ET bridge from MoO₄²⁻ to Eu³⁺ ions because the position of the energy level caused by MoO₄²⁻ absorption is close to that of Eu³⁺ excited states. When the In(OH)₃ content is high enough, the ET bridge function from CTB to Eu³⁺ ions becomes efficient. And thus, compared to NEM(I), the location of the total excitation peak after superposition red-shift first, and then reverse. In addition, the CTB Eu³⁺ \rightarrow O²⁻ of NEM(I)@In-x show blue-shift compared to NEM(I), indicating that the particle size of internal NaLn(MoO₄)₂ in NEM(I)@In-x is smaller than that in NEM(I). This further proves that NaLn(MoO₄)₂ nanoclusters can be effectively isolated by In $(OH)_3$ to form clusters, and then the ultra-small $NaLn(MoO_4)_2@In$ (OH)₃ clusters gradually self-assemble into hierarchical structures. Thus, the NaEu(MoO₄)₂@In(OH)₃ can be excited by the UV-blue light and emit green, yellow, orange, and red light, which could be used in III-nitride based white LEDs to achieve low-cost and high color quality white light emission.

It is an effective way to improve the luminescence quantum efficiency by suppressing the non-radiative transition and increasing the fluorescence lifetime of the metastable energy level of rareearth ions. Thus, the fluorescence decay curves of the NEM(I) and NEM(I)@In-x (x = 6, 9, 12) under 295 nm excitation were measured as shown in Fig. S22. The decay curves were fitted with a double exponential function and the average fluorescence lifetimes of

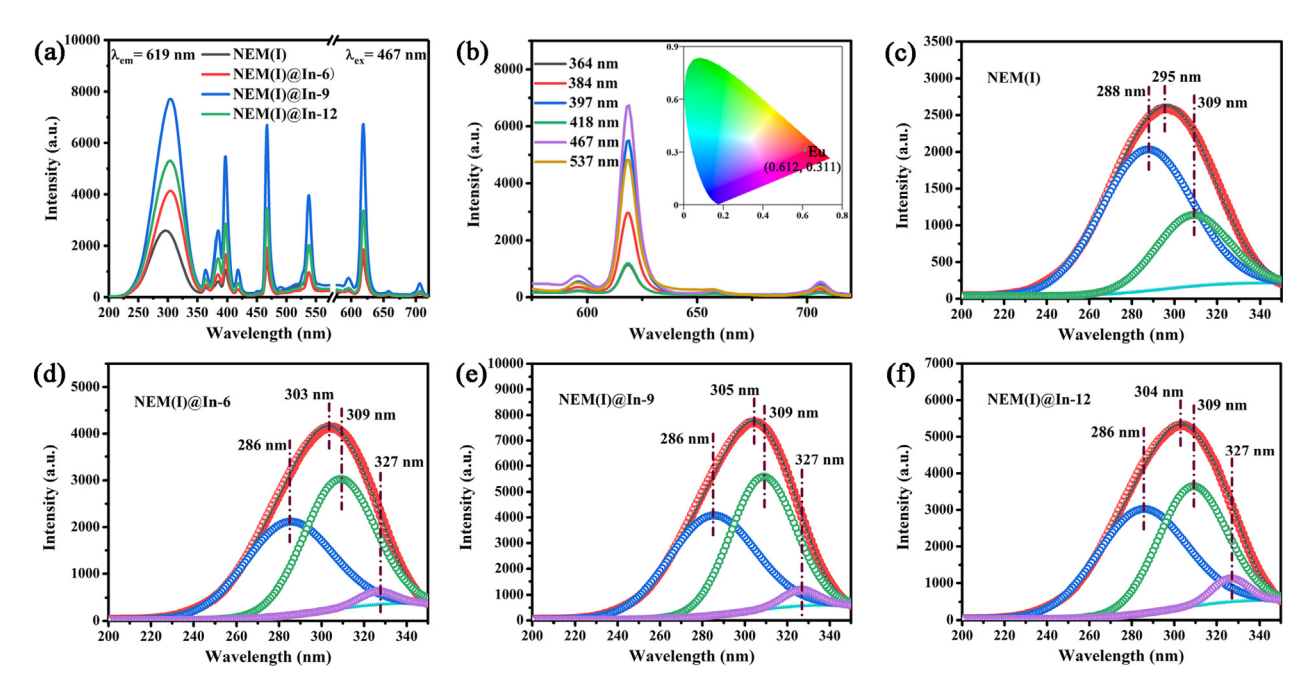


Fig. 2. (a) Excitation (λ_{em} = 619 nm) and emission (λ_{ex} = 467 nm) spectra of NEM(I) and NEM(I)@In-x (x = 6, 9, and 12). (b) The emission spectra of NEM(I)@In-9 with different excitation wavelengths. Inset shows the CIE chromaticity coordinates for the NEM(I)@In-9 under 290 nm excitation. The excitation bands of (c) NEM(I) and (d-f) NEM(I)@In-x (x = 6, 9, and 12) in the range of 220–350 nm can be fitted with two and three Gaussian curves, respectively.

Table 1The calculated J-O parameters from the emission spectra of different samples (Fig. 2a).

Samples	$\Omega_2~(imes 10^{-20}~\text{cm}^2)$	$\Omega_4(\times 10^{-20}~\text{cm}^2)$
NEM(I)	4.93	2.27
NEM(I)@In-6	5.73	1.60
NEM(I)@In-9	8.38	1.90
NEM(I)@In-12	7.64	1.76

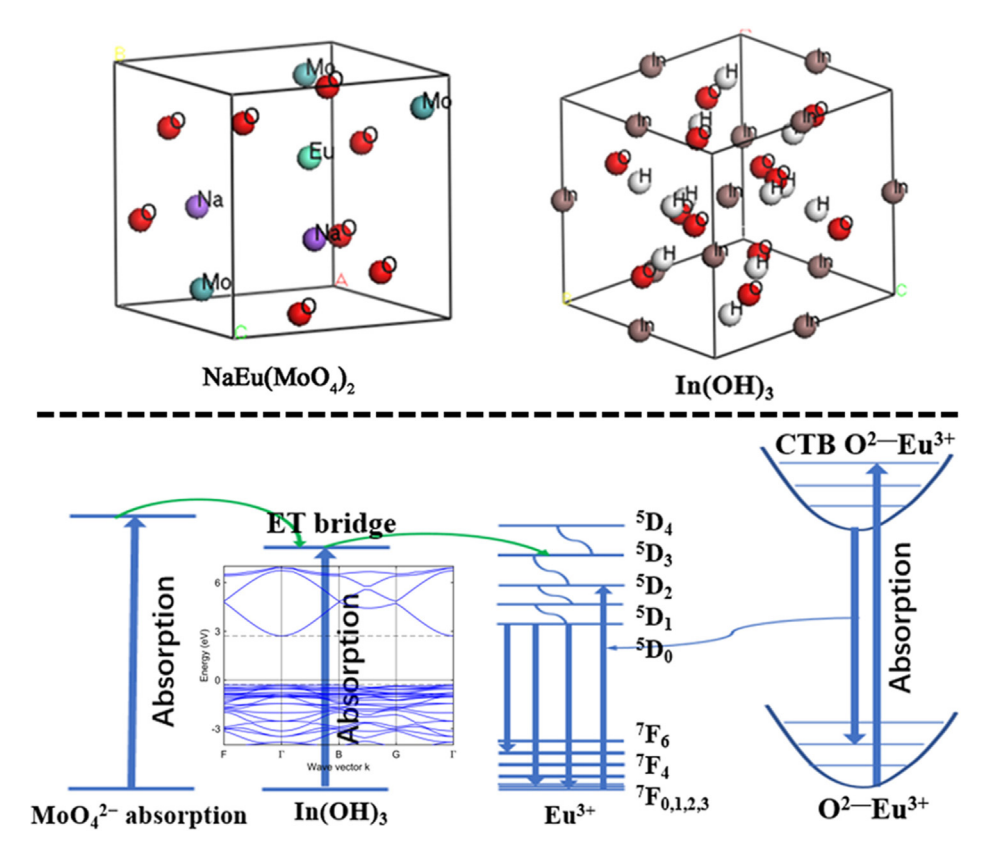
NEM(I), NEM(I)@In-6, NEM(I)@In-9, and NEM(I)@In-12 were calculated to be 23.282, 29.153, 52.658, and 46.684 μ s, respectively. Therefore, the fluorescence lifetime results can show that an appropriate amount of In(OH)₃ can effectively increase the lifetime as well as improve the luminescence quantum efficiency of NaLn (MoO₄)₂, which is consistent with the down-conversion spectra.

Subsequently, UC luminescence properties of the assynthesized NYME@In(OH)₃ hybrid nanostructures have also been investigated upon excitation by a 980-nm laser light, which displays the characteristic emission peaks of Er³⁺ ions (Fig. 3a). The spectra of the different hybrid nanostructures demonstrate two emission bands, which could be attributed to ${}^2H_{11/2}$ - ${}^4I_{15/2}$, ${}^4S_{3/2}$ $-{}^4I_{15/2}$ and ${}^4F_{9/2}$ - ${}^4I_{15/2}$ transitions of Er³⁺. Interestingly, upon gradually increasing molar amounts of In(OH)₃ from 0 to 0.8 mmol, the UC emission intensity was effectively enhanced, but further increasing the molar amounts to 1.2 mmol, the fluorescence of hybrid nanostructures was significantly quenched. In addition, the UC luminescence intensity of NYME(I)@In-8 hybrid nanostructures was enhanced nearly six times compared with NYME(I). More importantly, when NYME(I) was combined with In(OH)3, transitions from the $^4G_{11/2}$ (384 nm) and $^2H_{9/2}$ (411 nm) levels to the ground state of the Er $^{3+}$ ($^4I_{15/2}$) were observed. The enhanced UC luminescence of NYME@In(OH)₃ hybrid nanostructures can be related to the Raman peak signal at 134 cm⁻¹ originated from In -OH and the J-O parameters. It is well known that the excited states of Er3+ were populated by phonon-assisted energy transfer processes. Thus, the Raman peak signal at 134 cm⁻¹ related to In -OH is helpful to populate the excited states of Er³⁺, resulting in

stronger UC or DC emissions. On the other hand, the values of the I-O parameters also affect the intensity of the emission peaks of Er3+ ions. The UC emission spectra of NYME(I)@In-8 under 980-nm light excitation with different power densities are shown in Fig. 3b. The luminescence intensity of UC hybrid nanostructures could be also adjusted by changing the doping amounts of the Er³⁺ (Fig. 3c). As shown in Fig. S23, the influence of different temperatures on the UC luminescence of NYME (I) @ In-8 was studied. It can be seen from the illustration that the temperature has little effect on the luminous intensity. The CIE chromaticity coordinates of NYME(I)@In-8 were calculated to be (0.208, 0.755), as shown in Fig. S24. For comparison, the CIE chromaticity coordinates of all the samples were calculated, as shown in Table S1 and S2 in the ESI. In addition, the fluorescence intensity pump power dependence of NYME(I) (Fig. 3d) and NYME(I)@In-8 (Fig. 3e) was analyzed. The corresponding n values of the ${}^{2}H_{11/2}$ - ${}^{4}I_{15/2}$, ${}^{4}S_{3/2}$ - ${}^{4}I_{15/2}$ and ${}^{4}F_{9/2}$ - ${}^4I_{15/2}$ transitions of Er³⁺ from NYME(I)@In-8 are 2.05, 1.39, and 1.44, which explains that the ${}^{2}H_{11/2}$ - ${}^{4}I_{15/2}$ transitions may relate a three-photon process and the others (${}^4S_{3/2}$ - ${}^4I_{15/2}$ and ${}^4F_{9/2}$ -⁴I_{15/2}) are two-photon processes, as illustrated in Fig. 3e. The proposed energy transfer mechanism for the NYME@In(OH)3 hybrid nanostructures is illustrated in Fig. 3f.

3.4. Potential applications in white LEDs

The bright green, yellow, orange, and red emission obtained from NaLn(MoO₄)₂@In(OH)₃ could solve the issues challenging in the current generation white light-emitting diodes (LEDs). The current-generation white LEDs are typically obtained by coating a layer of yellow-emitting YAG: Ce³⁺ phosphors on the blue LED chips [52]. The high correlated color temperature (CCT) and low color rendering index (CRI) of white light due to the lack of red emission is not suitable for indoor lighting applications [53]. Recently, metal halide perovskites have been used to replace the yellow phosphors to achieve high-quality white light emission [54–57]. However, the red emission is obtained by using an I-based perovskites, which is hard to obtain and is easily decomposed in a very short time. Thus, in this work, the red emission



 $\textbf{Scheme 2.} \ \ \text{The top part is the structure diagrams of NaLn} (MOO_4)_2 \ \ \text{and } In(OH)_3. \ \ \text{The bottom part is the schematic for the ET and luminescence processes in NEM(I)@In-9.}$

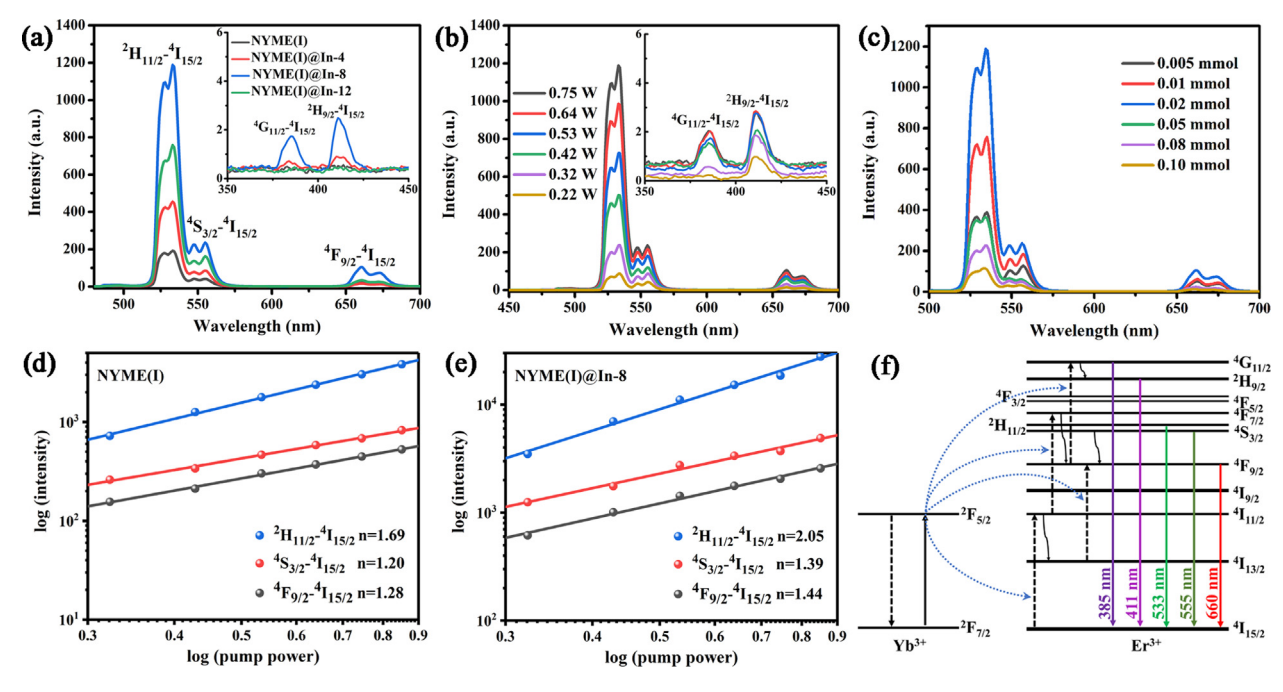


Fig. 3. (a) UC luminescence spectra of NYME(I) with different molar amounts of In(OH)₃ under 980 nm excitation. Inset shows the UC luminescence spectra of samples with 350–450 nm. (b) UC luminescence spectra of the NYME(I)@In-8 with different excitation powers. The inset shows the magnified spectra of NYME(I)@In-8, (c) UC spectra of NYME(I)@In-8 with different Er³⁺ concentrations. Plots (log–log) of the emission intensity versus pump power density of (d) NYME(I) and (e) NYME(I)@In-8. (f) The schematic illustration of the energy level and corresponding transitions.

from NaLn(MoO₄)₂@In(OH)₃ was combined with blue emission from CsZn_{0.15}Pb_{0.85}(Cl_{0.5}Br_{0.5})₃, green emission from CsZn_{0.15}Pb_{0.85}-Br₃, and yellow emission from CsZn_{0.15}Pb_{0.85}(Br_{0.5}I_{0.5})₃ to achieve the white light emission. The schematic white LED device structure

and emission spectra are shown in Fig. S25. We performed a systematic study on the effect of $NaLn(MoO_4)_2@In(OH)_3$ on color quality, vision performance, and heath effect of white light. By tuning the ratios of four different emissions, white light with superior

color quality, excellent vision performance, and dynamically adjustable CAF has been achieved. We have obtained the maximum LER of 376 lm/W through adjusting the power ratios of four different emissions to 1:1.8:1.9:4.1. Note that LER was calculated by using the following equation:

$$\textit{LER}(lm/W) = 683(lm/W) \frac{\int_{380}^{780} S_{total}(\lambda) V(\lambda) d\lambda}{\int_{380}^{780} S_{total}(\lambda) d\lambda} \tag{1}$$

where the $V(\lambda)$ is the luminous efficiency function (see the supporting information Fig. S26). The LER only depends on spectral power distributions (SPDs) $S_{total}(\lambda)$ and does not depends on the electrical properties of materials. Thus, the optimum LER can be obtained by engineering the spectral power distributions of white light. The luminous efficacy (LE) not only depends on the SPD but also depends on the electrical properties of materials. Therefore, LE is lower than LER. We achieved excellent LER by tuning the ratios of four different emissions. The corresponding CCT is 2989, which is warm white (see LED-A in Table 2). As a comparison, the use of red-emitting perovskites can only achieve the maximum LER of 318 lm/W [58]. Thus, the use of NaLn(MoO₄)₂@In(OH)₃ can achieve significantly high LER, and white light with excellent vision performance could be achieved. Furthermore, the white light with CCT of 5606 and CIE coordinates of (0.33, 0.34) has also been obtained, which is very close to the neutral white light. As a comparison, CIE coordinates of the standard neutral white light is (0.33, 0.33). We have also obtained white light with tunable CCT from warm white (CCT \sim 2989 K) to cold white (CCT \sim 9903 K) by engineering the power ratios of four different emissions and color characteristics of selected LEDs are shown in Table 2.

The corresponding spectral power distributions are shown in Fig. 4a and CIE coordinates of these LEDs are presented in Fig. 4b. Note that CRI is a parameter to evaluate the similarity of the light source colors compared to the blackbody source. It is primarily determined by the spectral power distributions of the light source. Thus, in this work, we engineered the spectral power distributions (SPD) of white light by tuning the ratios of four different emissions to achieve the extremely high CRI (up to 92.6). Based on the LED color characteristic datasheet published by the US Department of Energy (DOE), a light source with a CRI in the 90 s is excellent for indoor lighting applications [59]. Therefore, white light with excellent color quality has been achieved by combining NaLn (MoO₄)₂@In(OH)₃ with perovskite nanocrystals. The value of CRI was obtained by comparing the SPD of the light source with the blackbody radiation. The highest CRI which can be achieved is 100 when the SPD of the light source is the same as blackbody radiation. The value of LER was obtained by comparing the SPD of the light source with a luminous efficacy function. The maximum LER which can be achieved is 683 lm/W when the SPD of the light source is the same as the luminous efficacy function. Although both the CRI and LER were determined by the spectral power distributions (SPDs) of white light emission, there is a tradeoff between CRI and LER. We cannot obtain extra high CRI and LER at the same time. The white LEDs we obtained also have extremely small D_{uv} (0.0001–0.0009) compared to that of the fluorescence lamp (0.005) [60]. Therefore, white light with superior color quality, excellent vision performance, and tunable CCT can be achieved by combining NaLn(MoO₄)₂@In(OH)₃ with perovskite nanocrystals. The color-temperature tunable white light obtained by using NaLn (MoO₄)₂@In(OH)₃ as the components could lead to a variety of

Table 2Color characteristics of selected LEDs with tunable CCT from warm to cool white.

LEDs	Ratios (B:G:Y:R)	CCT (K)	Ra	CIE x	CIE y	Duv	LER (lm/W)	CAF
LED-A	1:1.8:1.9:4.1	2989	90.4	0.44	0.41	0.0007	376	0.36
LED-B	1:1.3:1.1:1.9	4002	92.2	0.38	0.38	0.0001	358	0.55
LED-C	1:1.0:0.6:1.1	5606	90.8	0.33	0.34	0.0007	328	0.78
LED-D	1:0.7:0.5:0.5	9903	92.6	0.28	0.29	0.0009	299	1.10

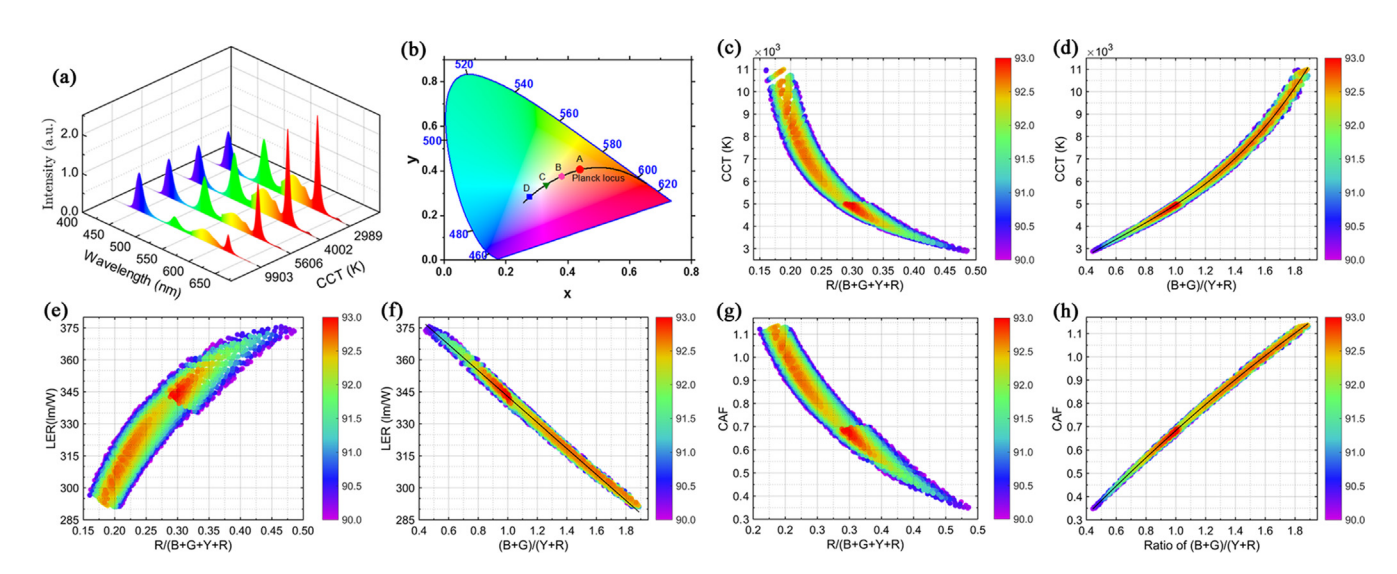


Fig. 4. (a) spectral power distribution of white light with various CCTs (2989–9903 K). (b) The chromaticity coordinates of white light in the CIE 1931 chromaticity diagram. (c) CCT changes with the ratio of red emission. (d) CCT with different relative power ratios of blue and green to yellow and red emissions. (e) The LER changes with the increase in the ratio of red emission. (f) LER as a function of ratios of blue and green emissions to yellow and red emissions. (g) CAF changes with power ratios of red emission. (h) CAF as a function of ratios of the sum of blue and green emissions to the sum of yellow and red emissions. The color bar indicates the CRI with corresponding CCT. (For interpretation of the references to color in this figure legend, the reader is referred to the web version of this article.)

applications including indoor and outdoor lighting. The low-cost and highly efficient white light emission with superior color quality will speed up the widespread adoption of white LED technology in the general illumination market and result in significant energy saving and budget-saving.

Furthermore, we also investigated the effect of $NaLn(MoO_4)_2@-In(OH)_3$ on the color quality, and vision performance, and health effect of white light. By increasing the amount of $NaLn(MoO_4)_2@-In(OH)_3$, the CCT and CAF of white light could be decreased and the LER could be increased as shown in Fig. 4(c, e, and g). The CCT, LER, and CAF dependency on the ratio (R) of blue and green emissions to yellow and red emissions are shown in Fig. 4(d, f, and h). They can be well fitted using the following functions:

$$CCT(R) = 850 + 5400R - 2750R^2 + 1461R^3 \tag{1}$$

$$LER(R) = 404 - 61R$$
 (2)

$$CAF(R) = 1.87 - 5.3R + 4.54R^2 \tag{3}$$

Thus, the LER linearly depends on the ratio of blue and green emissions to the yellow and red emissions. This provides guidelines for obtaining white light emission with excellent vision performance.

4. Conclusion

In summary, we successfully designed and synthesized NaLn (MoO₄)₂@In(OH)₃ hybrid nanostructures by a low-cost one-pot hydrothermal method. A series of characterization results show that NaLn(MoO₄)₂ ultra-small nucleus can be effectively isolated by In(OH)₃ to form NaLn(MoO₄)₂@In(OH)₃ composite nanoclusters because of the different nucleation rate between NaLn(MoO₄)₂ and In(OH)3, and then these small composite clusters gradually selfassemble into hierarchical structures. This is also the first report of the use of hydroxides to construct core-shell structures to enhance luminescence intensity. The morphology of the hybrid nanostructures can be engineered through the change of the solvent ratio in the reaction system. UC/DC luminescence intensity can be greatly enhanced by coating an appropriate amount of In $(OH)_3$ on $NaLn(MoO_4)_2$. The use of $In(OH)_3$ not only can increase the light absorption capability but also change the environment of Eu³⁺ which reflected from the change of J-O parameters. The coating of $In(OH)_3$ resulted in the greater Ω_2 , which directly contributed to the stronger intensity of 5D_0 - 7F_2 emission peak of Eu³⁺ ions. The coating of In(OH)₃ has also enhanced energy transfer from the charge transfer band (CTB) (Eu³⁺ \rightarrow O²⁻) to ⁵D₀ level or the excited states of Er³⁺ by phonon-assisted energy transfer processes which were evidenced by the presence of Raman peak signal at 134 cm⁻¹ (In–OH). This resulted in stronger UC or DC emissions. We also demonstrated that NaLn(MoO₄)₂@In(OH)₃ hybrid nanostructures could be used in white LEDs to achieve white light with excellent color quality and vision performance. Thus, NaLn (MoO₄)₂@In(OH)₃ hybrid nanostructures developed in this work are promising materials that can be used in bioimaging, lightemitting diodes (LEDs), and solid-state lasers.

CRediT authorship contribution statement

Guoyang Gao: Methodology, Software, Formal analysis, Investigation, Resources, Writing - review & editing, Writing - original draft. **Yini Li:** Validation, Formal analysis, Data curation. **Wenjing Yu:** Validation, Formal analysis. **Guofeng Wang:** Conceptualization, Methodology, Software, Formal analysis, Project administration, Writing - original draft, Visualization, Supervision. **Peifen**

Zhu: Conceptualization, Methodology, Software, Writing - review & editing, Writing - original draft, Investigation. **Weiping Qin:** Methodology, Formal analysis, Writing - original draft. **Dingsheng Wang:** Writing - original draft, Resources, Visualization.

Declaration of Competing Interest

The authors declare that they have no known competing financial interests or personal relationships that could have appeared to influence the work reported in this paper.

Acknowledgments

This work was supported by the National Natural Science Foundation of China (No. 21871079) and the National Science Foundation (No. 1945558).

Appendix A. Supplementary material

Supplementary data to this article can be found online at https://doi.org/10.1016/j.jcis.2020.09.049.

References

- W. Guan, W. Zhou, J. Lu, C. Lu, Luminescent films for chemo and biosensing, Chem. Soc. Rev. 44 (2015) 6981–7009.
- [2] Z. Xia, K.R. Poeppelmeier, Chemistry-inspired adaptable framework structures, Acc. Chem. Res. 50 (2017) 1222–1230.
- [3] F. Wang, Y. Han, C.S. Lim, Y. Lu, J. Wang, J. Xu, H. Chen, C. Zhang, M. Hong, X. Liu, Simultaneous phase and size control of upconversion nanocrystals through lanthanide doping, Nature 463 (2010) 1061–1065.
- [4] X. Xu, W. Zhang, D. Yang, W. Lu, J. Qiu, S.F. Yu, Phonon-assisted population inversion in lanthanide-doped upconversion Ba₂LaF₇ nanocrystals in glassceramics, Adv. Mater. 28 (2016) 8045–8050.
- [5] Y. Liu, M. Pan, Q. Yang, L. Fu, K. Li, S. Wei, C. Su, Dual-emission from a single-phase Eu–Ag metal–organic framework: an alternative way to get white-light phosphor, Chem. Mater. 24 (2012) 1954–1960.
- [6] M. Yu, H. Xu, Y. Li, Q. Dai, G. Wang, W. Qin, Morphology luminescence and photovoltaic performance of lanthanide doped CaWO₄ nanocrystals, J. Colloid Interf. Sci. 559 (2020) 162–168.
- [7] X. Wang, Q. Peng, Y. Li, Interface-mediated growth of monodispersed nanostructures, Acc. Chem. Res. 40 (2007) 635–643.
- [8] G. Pan, H. Song, X. Bai, Z. Liu, H. Yu, W. Di, S. Li, L. Fan, X. Ren, S. Lu, Novel energy-transfer route and enhanced luminescent properties in YVO₄:Eu³⁺/ YBO₃:Eu³⁺ Composite, Chem. Mater. 18 (2006) 4526–4532.
- [9] B. Cao, Y. Bao, Y. Liu, J. Shang, Z. Zhang, Y. He, Z. Feng, B. Dong, Wide-range and highly-sensitive optical thermometers based on the temperature-dependent energy transfer from Er to Nd in Er/Yb/Nd codoped NaYF₄ upconversion nanocrystals, Chem. Eng. J. 385 (2020) 123906.
- [10] Y. Sun, J. Zhang, Y. Chen, G. Yang, Porous lanthanide-organic open frameworks with helical tubes constructed from interweaving triple-helical and doublehelical chains, Angew. Chem. Int. Ed. 44 (2005) 5814–5817.
- [11] L. Liang, D.B.L. Teh, N.D. Dinh, W. Chen, Q. Chen, Y. Wu, S. Chowdhury, A. Yamanaka, T.C. Sum, C.H. Chen, N.V. Thakor, A.H. All, X. Liu, Upconversion amplification through dielectric superlensing modulation, Nat. Commun. 10 (2019) 1391.
- [12] S. Gai, C. Li, P. Yang, J. Lin, Recent progress in rare earth micro/nanocrystals: soft chemical synthesis, luminescent properties, and biomedical applications, Chem. Rev. 114 (2014) 2343–2389.
- [13] W. You, D. Tu, R. Li, W. Zheng, X. Chen, "Chameleon-like" optical behavior of lanthanide-doped fluoride nanoplates for multilevel anti-counterfeiting applications, Nano Res. 12 (2019) 1417–1422.
- [14] J. Xu, A. Gulzar, D. Yang, S. Gai, F. He, P. Yang, Tumor self-responsive upconversion nanomedicines for theranostic applications, Nanoscale 11 (2019) 17535–17556.
- [15] J. Miao, X. Duan, J. Li, J. Dai, B. Liu, S. Wang, W. Zhou, Z. Shao, Boosting performance of lanthanide magnetism perovskite for advanced oxidation through lattice doping with catalytically inert element, Chem. Eng. J. 355 (2019) 721–727.
- [16] W. Zheng, P. Huang, Z. Gong, D. Tu, J. Xu, Q. Zou, R. Li, W. You, J.C.G. Bünzli, X. Chen, Near-infrared-triggered photon upconversion tuning in all-inorganic cesium lead halide perovskite quantum dots, Nat. Commun. 9 (2018) 3462.
- [17] M. Yu, Y. Qu, K. Pan, G. Wang, Y. Li, Enhanced photoelectric conversion efficiency of dye-sensitized solar cells by the synergetic effect of NaYF₄:Er³⁺/ Yb³⁺ and g-C₃N₄, Sci. China Mater. 60 (2017) 228–238.
- [18] M. Zhang, W. Zheng, Y. Liu, P. Huang, Z. Gong, J. Wei, Y. Gao, S. Zhou, X. Li, X. Chen, A new class of blue-LED-excitable NIR-II luminescent nanoprobes based

- on lanthanide-doped CaS nanoparticles, Angew. Chem. Int. Ed. 58 (2019) 9556–9560.
- [19] Y. Wang, G. Liu, L. Sun, J. Xiao, J. Zhou, C. Yan, Nd³⁺-sensitized upconversion nanophosphors: efficient in vivo bioimaging probes with minimized heating effect, ACS Nano 7 (2013) 7200–7206.
- [20] M. Yu, J. Su, G. Wang, Y. Li, Pt/Y₂O₃:Eu³⁺ composite nanotubes: enhanced photoluminescence and application in dye-sensitized solar cells, Nano Res. 9 (2016) 2338–2346.
- [21] S.K. Gupta, J.P. Zuniga, M. Abdou, M.P. Thomas, M. De Alwis Goonatilleke, B.S. Guiton, Y. Mao, Lanthanide-doped lanthanum hafnate nanoparticles as multicolor phosphors for warm white lighting and scintillators, Chem, Eng. J. 379 (2020) 122314.
- [22] Y. Liu, W. Zhuang, Y. Hu, W. Gao, J. Hao, Synthesis and luminescence of sub-micron sized Ca₃Sc₂Si₃O₁₂: Ce green phosphors for white light-emitting diode and field-emission display applications, J. Alloy. Compd. 504 (2010) 488–492.
- [23] J. Shen, Y. Li, H. Zhao, K. Pan, X. Li, Y. Qu, G. Wang, D. Wang, Modulating the photoelectrons of g-C₃N₄ via coupling MgTi₂O₅ as appropriate platform for visible-light-driven photocatalytic solar energy conversion, Nano Res. 12 (2019) 1931–1936.
- [24] Y. Zhang, L. Zhang, R. Deng, J. Tian, Y. Zong, D. Jin, X. Liu, Multicolor barcoding in a single upconversion crystal, J. Am. Chem. Soc. 136 (2014) 4893–4896.
- [25] Y. Fang, A. Xu, R. Song, H. Zhang, L. You, J.C. Yu, H. Liu, Systematic synthesis and characterization of single-crystal lanthanide orthophosphate nanowires, J. Am. Chem. Soc. 125 (2003) 16025–16034.
- [26] F. Li, X. Wang, Z. Xia, C. Pan, Q. Liu, Photoluminescence tuning in stretchable PDMS film grafted doped core/multishell quantum dots for anticounterfeiting, Adv. Funct. Mater. 27 (2017) 1700051.
- [27] H. Huang, J. Chen, Y. Liu, J. Lin, S. Wang, F. Huang, D. Chen, Lanthanide-doped core@multishell nanoarchitectures: multimodal excitable upconverting/downshifting luminescence and high-level anti-counterfeiting, Small 16 (2020) 2000708.
- [28] W. Ren, S. Wen, S.A. Tawfik, Q.P. Su, G. Lin, L.A. Ju, M.J. Ford, H. Ghodke, M. van Antoine, D.J. Oijen, Anisotropic functionalization of upconversion nanoparticles, Chem. Sci. 9 (2018) 4352–4358.
- [29] R. Qiao, H. Qiao, Y. Zhang, Y. Wang, C. Chi, J. Tian, L. Zhang, F. Cao, M. Gao, Molecular imaging of vulnerable atherosclerotic plaques in vivo with osteopontin-specific upconversion nanoprobes, ACS Nano 11 (2017) 1816– 1825.
- [30] B. Zhou, B. Shi, D. Jin, X. Liu, Controlling upconversion nanocrystals for emerging applications, Nat. Nanotechnol. 10 (2015) 924–936.
- [31] J. Gomez-Morales, C. Verdugo-Escamilla, R. Fernandez-Penas, C.M. Parra-Milla, C. Drouet, M. Iafisco, F. Oltolina, M. Prat, J.F. Fernandez-Sanchez, Bioinspired crystallization, sensitized luminescence and cytocompatibility of citratefunctionalized Ca-substituted europium phosphate monohydrate nanophosphors, J. Colloid Interf. Sci. 538 (2019) 174-186.
- [32] A. Gulzar, J. Xu, P. Yang, F. He, L. Xu, Upconversion processes: versatile biological applications and biosafety, Nanoscale 9 (2017) 12248–12282.
- [33] Y. Liu, D. Wang, L. Li, Q. Peng, Y. Li, Energy upconversion in lanthanide-doped core/porous-shell nanoparticles, Inorg. Chem. 53 (2014) 3257–3259.
- [34] J. Zhou, Q. Liu, W. Feng, Y. Sun, F. Li, Upconversion luminescent materials: advances and applications, Chem. Rev. 115 (2015) 395–465.
- [35] S. Wen, J. Zhou, K. Zheng, A. Bednarkiewicz, X. Liu, D. Jin, Advances in highly doped upconversion nanoparticles, Nat. Commun. 9 (2018) 12.
- [36] G. Chen, H. Ågren, T.Y. Ohulchanskyy, P.N. Prasad, Light upconverting coreshell nanostructures: nanophotonic control for emerging applications, Chem. Soc. Rev. 44 (2015) 1680–1713.
- [37] B. Huang, J. Bergstrand, S. Duan, Q. Zhan, J. Widengren, H. Ågren, H. Liu, Overtone vibrational transition-induced lanthanide excited-state quenching in Yb³⁺/Er³⁺-doped upconversion nanocrystals, ACS Nano 12 (2018) 10572– 10575.
- [38] B. Ding, S. Shao, H. Xiao, C. Sun, X. Cai, F. Jiang, X. Zhao, P.a. Ma, J. Lin, MnFe₂O₄-decorated large-pore mesoporous silica-coated upconversion nanoparticles for near-infrared light-induced and O₂ self-sufficient photodynamic therapy, Nanoscale 11 (2019) 14654–14667.
- [39] Y. Ji, W. Xu, D. Li, D. Zhou, X. Chen, N. Ding, J. Li, N. Wang, X. Bai, H. Song, Semiconductor plasmon enhanced monolayer upconversion nanoparticles for high performance narrowband near-infrared photodetection, Nano Energy 61 (2019) 211–220.

- [40] D. Chen, L. Liu, P. Huang, M. Ding, J. Zhong, Z. Ji, Nd³⁺-sensitized Ho³⁺ single-band red upconversion luminescence in core–shell nanoarchitecture, J. Phys. Chem. Lett. 6 (2015) 2833–2840.
- [41] W. Xu, Y. Zhu, X. Chen, J. Wang, L. Tao, S. Xu, T. Liu, H. Song, A novel strategy for improving upconversion luminescence of NaYF₄: Yb, Er nanocrystals by coupling with hybrids of silver plasmon nanostructures and poly(methyl methacrylate) photonic crystals, Nano Res. 6 (2013) 795–807.
- [42] Y. Li, J. Tang, L. He, Y. Liu, Y. Liu, C. Chen, Z. Tang, Core-Shell upconversion nanoparticle@metal-organic framework nanoprobes for luminescent/magnetic dual-mode targeted imaging, Adv. Mater. 27 (2015) 4075–4080.
- [43] S. Ye, G. Chen, W. Shao, J. Qu, P.N. Prasad, Tuning upconversion through a sensitizer/activator-isolated NaYF₄ core/shell structure, Nanoscale 7 (2015) 3976–3984.
- [44] J. Li, X. Li, X. Sun, T. Ishigaki, Monodispersed colloidal spheres for uniform Y₂O₃:Eu³⁺ red-phosphor particles and greatly enhanced luminescence by simultaneous Gd³⁺ doping, J. Phys. Chem. C 112 (2008) 11707–11716.
- [45] D.J. Garfield, N.J. Borys, S.M. Hamed, N.A. Torquato, C.A. Tajon, B. Tian, B. Shevitski, E.S. Barnard, Y.D. Suh, S. Aloni, J.B. Neaton, E.M. Chan, B.E. Cohen, P.J. Schuck, Enrichment of molecular antenna triplets amplifies upconverting nanoparticle emission, Nat. Photonics 12 (2018) 402–407.
- [46] F. Wang, R. Deng, J. Wang, Q. Wang, Y. Han, H. Zhu, X. Chen, X. Liu, Tuning upconversion through energy migration in core-shell nanoparticles, Nat. Mater. 10 (2011) 968–973.
- [47] J. Xu, M. Sun, Y. Kuang, H. Bi, B. Liu, D. Yang, R. Lv, S. Gai, F. He, P. Yang, Markedly enhanced up-conversion luminescence by combining IR-808 dye sensitization and core-shell-shell structures, Dalton Trans. 46 (2017) 1495–
- [48] B. Hu, M. Hu, Q. Guo, K. Wang, X. Wang, In-vacancy engineered plate-like In (OH)₃ for effective photocatalytic reduction of CO₂ with H₂O vapor, Appl. Catal. B: Environ. 253 (2019) 77–87.
- [49] S.C.S. Lemos, E. Nossol, J.L. Ferrari, E.O. Gomes, J. Andres, L. Gracia, I. Sorribes, R. C. Lima, Joint theoretical and experimental study on the La doping process in In₂O₃: phase transition and electrocatalytic activity, Inorg. Chem. 58 (2019) 11738–11750.
- [50] W. Maisang, A. Phuruangrat, S. Thongtem, T. Thongtem, Photoluminescence and photonic absorbance of Ce₂(MoO₄)₃ nanocrystal synthesized by microwave-hydrothermal/solvothermal method, Rare Met. 37 (2018) 868– 874.
- [51] A. Ćirić, S. Stojadinović, M. Sekulić, M.D. Dramićanin, JOES: An application software for Judd-Ofelt analysis from Eu³⁺ emission spectra, J. Lumin. 205 (2019) 351–356.
- [52] M.R. Krames, O.B. Shchekin, R. Mueller-Mach, G.O. Mueller, Z. Ling, G. Harbers, M.G. Craford, Status and future of high-power light-emitting diodes for solidstate lighting, J. Disp. Technol. 3 (2007) 160–175.
- [53] X. Li, J.D. Budai, F. Liu, J.Y. Howe, J. Zhang, X.J. Wang, Z. Gu, C. Sun, R.S. Meltzer, Z. Pan, New yellow Ba_{0.93}Eu_{0.07}Al₂O₄ phosphor for warm-white light-emitting diodes through single-emitting-center conversion, Light Sci. Appl. 2 (2013) e50.
- [54] D. Chen, X. Chen, Luminescent perovskite quantum dots: synthesis, microstructures, optical properties and applications, J. Mater. Chem. C 7 (2019) 1413–1446.
- [55] J. Zhu, Z. Xie, X. Sun, S. Zhang, G. Pan, Y. Zhu, B. Dong, X. Bai, H. Zhang, H. Song, Highly efficient and stable inorganic perovskite quantum dots by embedding into a polymer matrix, ChemNanoMat 5 (2019) 346–351.
- [56] R. F. Service, Perovskite LEDs begin to shine, Science 364 (2019) 918.
- [57] D. Chen, Y. Liu, C. Yang, J. Zhong, S. Zhou, J. Chen, H. Huang, Promoting photoluminescence quantum yields of glass-stabilized CSPbX₃ (X = Cl, Br, I) perovskite quantum dots through fluorine doping, Nanoscale 11 (2019) 17216–17221.
- [58] S. Thapa, G.C. Adhikari, H. Zhu, A. Grigoriev, P. Zhu, Zn-alloyed all-inorganic halide perovskite-based white light-emitting diodes with superior color quality, Sci. Rep. 9 (2019) 18636.
- [59] Solid-State Lighting Technology Fact Sheet-LED Color Characteristics, https:// www.energy.gov/sites/prod/files/2016/08/f33/led-color-characteristicsfactsheet.pdf.
- [60] Y. Ohno, Spectral design considerations for white LED color rendering, Opt. Eng. 44 (2005) 9.